IEEE Photonics Journal
An IEEE Photonics Society Publication

Open Access

A Low-Voltage 35-GHz Silicon Photonic Modulator-Enabled 112-Gb/s Transmission System

Volume 7, Number 3, June 2015

Alireza Samani
Mathieu Chagnon
David Patel
Venkat Veerasubramanian
Samir Ghosh
Mohamed Osman
Qiuhang Zhong
David V. Plant

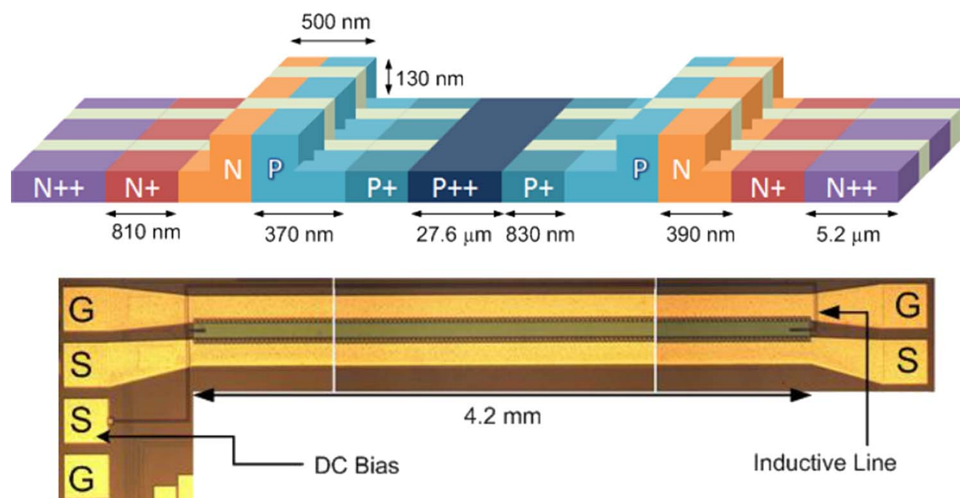

DOI: 10.1109/JPHOT.2015.2426875
1943-0655 © 2015 IEEE

IEEE photonics SOCIETY

IEEE

A Low-Voltage 35-GHz Silicon Photonic Modulator-Enabled 112-Gb/s Transmission System

Alireza Samani, Mathieu Chagnon, David Patel, Venkat Veerasubramanian, Samir Ghosh, Mohamed Osman, Qiuhang Zhong, and David V. Plant

Department of Electrical and Computer Engineering, McGill University, Montréal, QC H3A 0G4, Canada

DOI: 10.1109/JPHOT.2015.2426875
1943-0655 © 2015 IEEE. Translations and content mining are permitted for academic research only. Personal use is also permitted, but republication/redistribution requires IEEE permission. See http://www.ieee.org/publications_standards/publications/rights/index.html for more information.

Manuscript received March 31, 2015; accepted April 21, 2015. Date of publication April 28, 2015; date of current version May 6, 2015. This work was supported by the Natural Sciences and Engineering Research Council of Canada, CREATE Si-EPIC, TeraXion, PROMPT, and CMC Microsystems. Corresponding author: A. Samani (e-mail: alireza.samani@mail.mcgill.ca).

Abstract: We present a silicon photonic traveling-wave Mach–Zehnder modulator operating near 1550 nm with a 3-dB bandwidth of 35 GHz. A detailed analysis of traveling-wave electrode impedance, microwave loss, and phase velocity is presented. Small- and large-signal characterization of the device validates the design methodology. We further investigate the performance of the device in a short-reach transmission system. We report a successful 112-Gb/s transmission of four-level pulse amplitude modulation over 5 km of SMF using 2.2 V_{p-p} drive voltage. Digital signal processing is applied at the transmitter and receiver. 56-GBaud PAM-4 and 64-Gb/s PAM-2 transmission is demonstrated below a pre-FEC hard decision threshold of 4.4×10^{-3}.

Index Terms: Silicon nanophotonics, electrooptical systems, microwave photonics signal processing.

1. Introduction

The constant spread of cloud services offered by data centers (DCs) and the increasing demand for higher bandwidth driven by web-based applications and services have increased the need for faster and inexpensive short-reach optic solutions [1].

Because of the compatibility with the proven CMOS manufacturing process, silicon photonics (SiP) is a promising technology capable of supporting 100 Gb/s, and later 400 Gb/s, intra-data center connectivity requirements ranging from 0.5 to 10 km. Currently, 100 Gb/s transmission of Ethernet frames over SMF used in DCs is realized using a 4 $\times$ 25 Gb/s, WDM format [2]. However, it is widely accepted that the 400 Gb/s systems will be realized using a 4 $\times$ 100 Gb/s configuration, which necessitates the need to achieve single wavelength operation at 100 Gb/s [3]. SiP based optoelectronic devices have shown to provide energy efficient, low cost and high bandwidth solution for coherent links [4]–[6] and short-reach optical interconnects [7], [8].

High speed modulators are key SiP building blocks. High-speed ring modulators have gained immense interest recently, achieving ultra-low modulation power consumption. However, these modulators suffer from limited optical bandwidth and strict wavelength dependence and consequently a stringent need for thermal stabilization [9]. Mach–Zehnder SiP modulators are candidate devices for achieving these data rates because of their large bandwidths. Traveling wave

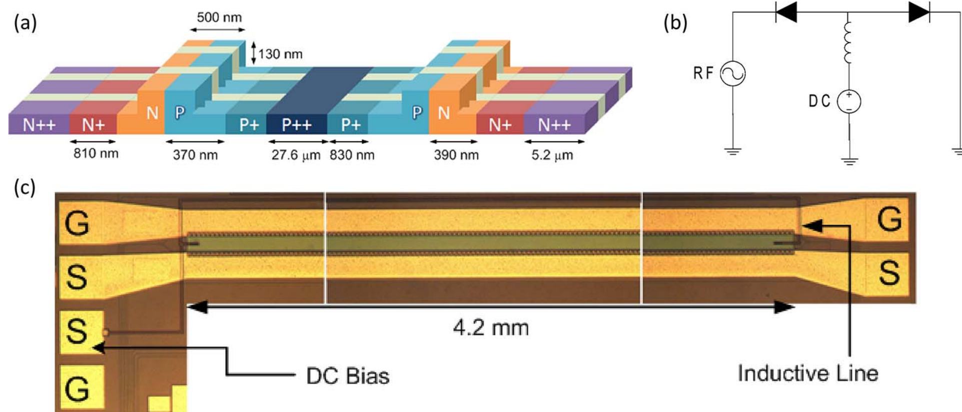

Fig. 1. (a) Cross section of the PN junctions in the series push–pull configuration, (b) equivalent DC circuit schematic of modulation section, and (c) micrograph of the TW-MZM.

Mach–Zehnder modulators (TW-MZM) are currently used in commercial systems because of their thermal insensitivity and tolerance to fabrication imperfections.

To achieve higher data rate transmission, advanced optical modulation formats together with polarization and wavelength division multiplexing are required. Pulse amplitude modulation (PAM) enables higher spectral efficiency by using multi-level amplitudes. Using a PAM-4 modulation format doubles the spectral efficiency of the optical link. Recently, PAM generation has been demonstrated using SiP intensity modulators [7], [10], and [11].

In this paper, we present a 4.2 mm long, single drive series push–pull (SPP) SiP traveling wave Mach–Zehnder modulator (TW-MZM) with 3 dB bandwidth of 35 GHz bandwidth based on a lateral PN junction operating near 1550 nm. The $V_\pi L_\pi$ of the more efficient phase shifter is 3.15 V-cm, and the small signal V_π is 7.5 V. The insertion loss of the device excluding the grating couplers loss is 4.5 dB. To the best of our knowledge this modulator surpasses the highest bandwidth reported for a SiP modulator by 5 GHz [12]. At a similar length and bandwidth, the reported device achieves the lowest reported V_π. A bit rate of 112 Gb/s is achieved using PAM-4 modulation at 56 Gbaud after 5 km of single mode fiber (SMF) below the hard decision pre-FEC threshold of 4.4×10^{-3} [13] to provide a final bit error rate under 10^{-15}. A detailed analysis of the traveling wave electrode including design procedure to achieve impedance and velocity matching is presented.

2. Device Design and Fabrication

The purpose of a transverse traveling wave modulator is to accumulate phase modulation monolithically using a RF modulating wave that propagates at the same speed and same direction as the optical wave. Optical and microwave design considerations of the TW-MZM are explained in the following two sections.

2.1 Fabrication Process and PN Junction Design

The TW-MZM was fabricated in a 220 nm silicon-on-insulator (SOI) technology on a 300 mm SOI wafer with 2 μm buried oxide via a Multi Project Wafer (MPW) shuttle run. The reported MZM is designed to operate near the 1550 nm wavelength and is based on a single drive series push–pull scheme where the PN junctions embedded in each arm are connected in series with opposite polarity [14], as illustrated in Fig. 1. An equivalent 1310 nm device is easily realized with minor changes to waveguide width to allow single mode optical wave propagation. Intermediate P+ and N+ doping levels with implantation densities of $2 \times 10^{18}/\text{cm}^{-3}$ and $3 \times 10^{18}/\text{cm}^{-3}$ are used to reduce the series resistance without significantly increasing optical propagation

loss. Highly doped P++ and N++ levels with concentration of $1 \times 10^{20}/\mathrm{cm}^{-3}$ are used for ohmic contact formation. The PN junctions in series will have a reduced capacitance at the expense of higher resistance. However the microwave loss is reduced as a result of the lower capacitance, allowing the SPP modulators to achieve higher bandwidth compared to conventional differential drive modulators. This configuration allows the modulator to be driven by a single RF input compared to differential drive signals needed in conventional dual drive schemes at the expense of slightly larger drive voltages [15]. Fig. 1(b) illustrates a simplified equivalent circuit of the SPP configuration. The DC bias voltage is applied to the common P-doped region between the two PN junctions using an on-chip 5 mm-long inductive line to ensure that the PN junctions operate in reverse bias at all times. This biasing scheme isolates DC current from the 50 Ω electrode matching termination. Fig. 1(c) shows a micrograph of the TW-MZM. The width of Si waveguide in each arm is 500 nm, and the rib and slab thicknesses are 220 and 90 nm, respectively. Compact Y-branches are used at both ends of the TW-MZM as input/output 3-dB splitter/combiners. The length of each arm of the TW-MZM is 4.2 mm, and the total electrode length is 4.7 mm. An imbalance of 100 μm is used to achieve a free spectral range of approximately 5 nm. The PN junctions embedded in the waveguides are divided into 9 μm segments with 1.5 μm intrinsic spaces [shown in cream color in Fig. 1(a)], which results in a 85% filling factor. This prevents any current flowing through silicon as illustrated in Fig. 1(a). This will result in an effective phase shifter length of 3.6 mm for each arm. The capacitance of the PN junction (C_{PN}) is calculated using device simulation software and is strictly dependent on the doping concentration values, geometry of optical waveguides and DC bias voltage. At 0 V DC C_{PN} is simulated to be 230 fF/μm and under a 3 V DC bias this value drops to 170 fF/μm. Using the above doping values, the simulated V_π of the TW-MZM is 6 V. Hence, a DC bias voltage of 3 V will ensure that the PN junctions are always reverse biased when the modulator is driven by the maximum driving voltage of 6 V_{p-p}. However, to achieve an error-free modulation, using the maximum driving voltage is not necessary and the modulator can be driven by lower driving voltages, as long as $V_{DC} \geq V_{p-p}/2$.

2.2 Quasi-Analytical Analysis of Traveling Wave Electrodes

Longer TW-MZMs are more desirable because they can achieve a π phase shift with lower driving voltages. However, due to the lossy silicon substrate, the PN junction capacitance and the difference between microwave refractive index and optical wave refractive index, achieving a high electro-optic (E-O) bandwidth is particularly challenging. To maximize the E-O frequency response of the modulator three design criteria should be considered: (a) The modulator's characteristic impedance should match the impedance of the RF driver and termination, (b) the RF losses of the modulator should be minimized, and (c) the mismatch between the optical group velocity and RF phase velocity should be minimized [16]. Depending on the microwave signal spectrum and the silicon substrate doping concentration, the microwave signal propagates along the traveling wave electrodes in either quasi-TEM mode, skin effect mode, or slow wave mode [17].

The coplanar strip (CPS) configuration is used to form the traveling wave electrode of the modulator. All of the above mentioned criteria can be realized using a CPS electrode [18]. However, to have further control on the RF phase velocity and microwave loss, slow wave electrode structures can be used. Slow wave structures can be realized by periodic inductive or capacitive loading of the CPS line [19]–[21] or using shielded coplanar waveguide geometries. However due to the smaller feature sizes of these electrodes, they are more sensitive to fabrication and in general occupy more than twice the area required by simple coplanar strips of the same length [20]. Moreover, due to the PN junction capacitance, the highly doped regions between the two arms of the MZM, and the multilayer substrate structure, the microwave traveling along the electrodes propagates in slow-wave mode making special inductive or loaded electrode structures unnecessary [22].

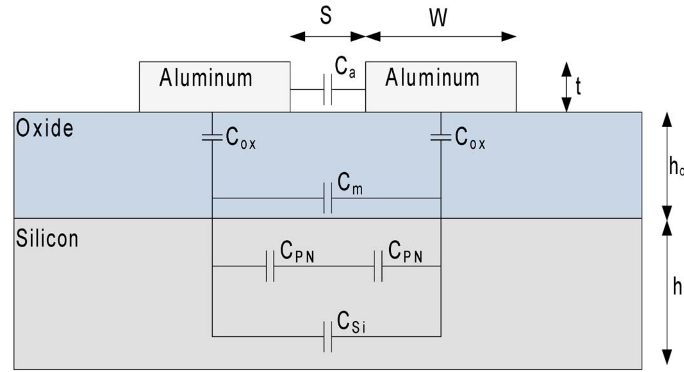

Fig. 2. Cross section of the coplanar strip configuration on the SOI substrate.

2.2.1 Impedance Matching

Since most commercial RF drivers and test equipment are designed to have a 50 Ω impedance, it is important for the TW-MZM to have a characteristic impedance of 50 Ω to avoid back reflection of the RF signal which could cause inter symbol interference (ISI) and higher microwave insertion loss. Fig. 2 shows a symmetric CPS line on finite thickness multilayered substrate.

The characteristic impedance and effective relative dielectric constant of the CPS line with a substrate thickness h and metal trace thickness t on a lightly doped silicon substrate can be obtained by [23]

$$Z_0 = \frac{120\pi}{\sqrt{\varepsilon_{re}}} \frac{K(k_0)}{K(k_0')} \tag{1}$$

$$\varepsilon_{re} = \frac{C_a + C_s}{C_a} \tag{2}$$

where C_a and C_s are capacitances contributed by the electric field in the air and the substrate region, respectively; K is the complete elliptic integral of the first kind; and $k_0 = S/(S + 2W)$. The above expression for ε_{re} is only valid for lightly doped homogenous silicon substrates. We can extend the above expressions to accurately model the behavior of the CPS lines for the multi-level substrate of the SOI platform, including the highly doped silicon regions and the PN junction capacitance. To calculate the characteristic impedance and effective dielectric constant of the CPS line, we expand the total substrate capacitance (C_s) used in (2) to include PN junction capacitance (CPN), and the capacitive coupling through the oxide layer (C_m), the silicon substrate capacitance (C_{si}), and the capacitance between the metal traces and the bulk oxide substrate (C_{ox}) which is shown in series. As shown in Fig. 2, when the CPS line is loaded with the PN junctions, the added capacitance, CPN, will affect the relative effective dielectric constant and the characteristic impedance of the CPS lines by increasing the substrate capacitance C_s. In addition the buffer oxide layer between the metal traces and the silicon substrate has a lower relative permittivity compared to that of silicon and its addition will decrease the total substrate capacitance (C_s) and therefore C_{ox} is generally shown as connected in series [24]–[26]. The position of the oxide layer and its different permittivity will create geometry and voltage dependent capacitances C_m and C_{ox} that will affect the total substrate capacitance Cs value. C_m and C_{ox} are calculated using the Green's function method shown in [26] and [16] and are dependent on electrode geometries (W, S, and t), oxide layer thickness (h_0) and relative permittivity of oxide. As shown in Fig. 2, the silicon substrate and electrode traces are separated by the oxide buffer layer. This will result in lower electric field intensity in the silicon substrate. Therefore, in addition to electrode geometry, silicon substrate thickness (h) and permittivity, C_{si} is dependent on oxide layer thickness as well. The CPN value at 3 V DC bias is used in the calculations since this will ensure that the device will be operated in reverse bias at all times as mentioned previously. However, a DC biasing voltage $V_{DC} \geq V_{p-p}/2$ can be used when the modulator is driven with

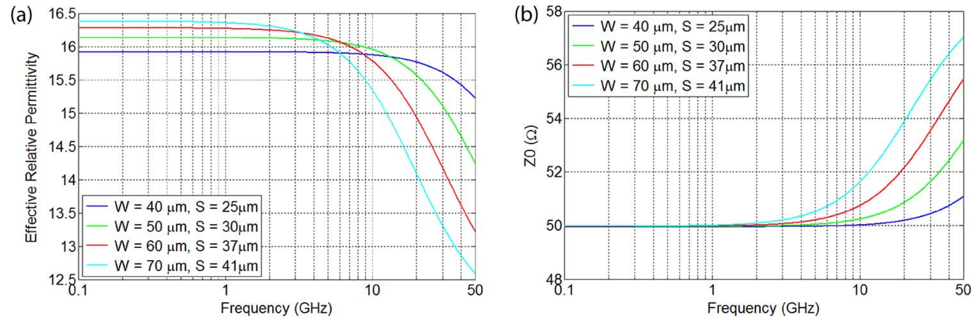

Fig. 3. (a) Effective dielectric constant versus frequency and (b) characteristic impedance of PN junction loaded CPS lines vs. frequency.

V_{p-p} lower than the required V_π. In the SPP configuration, the two PN junctions are connected in series. The equivalent capacitance of the two PN junctions at 3 V DC bias is simulated to be 85 pF/mm and is assumed to be independent of electrode geometry. The total substrate capacitance (C_s) resulting in $Z_0 = 50\ \Omega$ is calculated to be $C_s \sim 278$ pF/mm and $C_a \sim 18.7$ pF/mm for $k_0 \sim 0.23$ which indicates the capacitance of PN junction constitutes about 30% of the total substrate capacitance. Several different electrode geometries will result in a characteristic impedance of 50 Ω.

Equation (2) is based on quasi-static value of ε_{re} and does not include frequency dependence of ε_{re}. For higher frequency applications, the effects of dispersion on ε_{re} can be expressed as [27]

$$\sqrt{\varepsilon_{re}(f)} = \sqrt{\varepsilon_{re}} + \frac{\sqrt{\varepsilon_r} - \sqrt{\varepsilon_{re}}}{1 + m\left(\frac{f}{f_{TE}}\right)^{-1.8}} \tag{3}$$

where f_{TE} is the cutoff frequency for TE_0, and m is a fitting parameter obtained in [28]. The effective relative permittivity and characteristic impedance of a CPS line as a function of frequency are illustrated in Fig. 3. Several electrode width (W) and spacing (S) ratios achieve the target impedance matching of 50 Ω, however wider CPS traces suffer from impedance dispersion more severely at higher frequencies. Moreover the effective relative permittivity of the multi-layered substrate is shown to be higher than the relative permittivity of silicon $(\varepsilon_r = 11.9)$. This will result in lower microwave phase velocity, which will be discussed in Section 2.2.3.

2.2.2 Microwave Losses

To further optimize the traveling wave electrode, the microwave loss of the CPS line should be considered. Three main mechanisms contribute to microwave losses of CPS structures: (a) conductor losses of metal traces, (b) semiconductor dielectric losses including interface losses caused by charge carriers in the PN junctions and the highly doped silicon regions, and (c) radiation losses. Radiation losses are negligible for our proposed geometries and the total loss can be calculated as the sum of conductor and dielectric losses.

The conductor loss of a CPS line can be calculated as [29]

$$\alpha_c = \frac{8.68 R_s b^2}{16 Z_0 K^2(k_0)(b^2 - a^2)} \left\{ \frac{1}{a} \ln\left[\left(\frac{2a}{\Delta}\right)\left(\frac{b-a}{b+a}\right)\right] + \frac{1}{b} \ln\left[\left(\frac{2b}{\Delta}\right)\left(\frac{b-a}{b+a}\right)\right] \right\} \tag{4}$$

$$k_0 = \frac{S}{S + 2W} \tag{5}$$

$$a = \frac{S}{2} \tag{6}$$

$$b = W + S/2 \tag{7}$$

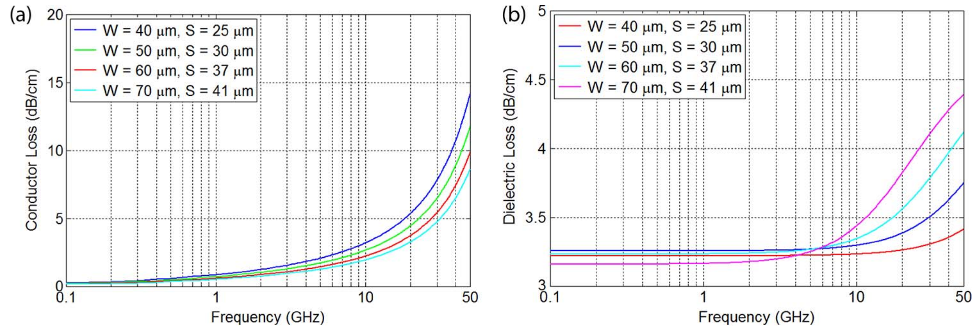

Fig. 4. (a) Conductor loss of a CPS line vs. frequency and (b) dielectric loss of a CPS line versus frequency.

where R_s is the frequency dependent surface resistance, Δ is skin depth dependent stopping distance tabulated in [23] for different geometries of CPS lines and K is the complete elliptic integral of the first kind. Conductor losses have strong frequency dependence and at frequencies above 20 GHz it is the dominant loss mechanism limiting the frequency response of the CPS line. Fig. 4(a) illustrates the conductor losses of CPS lines as a function of frequency for different values of W and S in Fig. 2. It can be observed that wider electrode geometries experience smaller microwave loss compared to narrower electrodes.

Similarly, the dielectric losses of CPS lines on doped silicon can be calculated as [23]

$$\alpha_d = 8.68\pi \frac{\varepsilon_r}{\sqrt{\varepsilon_{re}}} \left[\frac{\varepsilon_{re} - 1}{\varepsilon_r - 1}\right] \frac{tan\delta}{\lambda_0} \tag{8}$$

where $tan\delta$ is the loss tangent of the substrate and λ_0 is the wavelength in the transmission line. The effects of PN junction capacitance, oxide layer capacitance, and silicon and oxide interface are included in ε_{re} and $tan\delta$. Interface losses are caused by charge carriers at the Si/SiO_2 interface. When an oxide layer is present between the metal traces and the silicon substrate under an applied bias voltage, the CPS line behaves as a metal oxide semiconductor (MOS) varactor [28], which in turn increases Cox as the biasing voltage increases. For our calculations, we assume device operation at 3 V reverse bias. This will ensure that the PN junctions are always in reversed bias mode. Dielectric losses of the CPS lines under 3 V reverse bias for different widths and spacings are presented in Fig. 4(b). It is observed that dielectric loss is the dominant loss mechanism for frequencies below 20 GHz.

The total loss of the CPS line can be computed as the sum of conductor and dielectric losses. Assuming perfect impedance matching, i.e., no return loss, and ideal optical and microwave velocity matching, the calculated 3 and 6.4 dB EE bandwidth of a 4.2 mm long modulator limited by propagation loss using $|S_{21}| = e^{-\alpha L}$ is 25 GHz, and 39 GHz respectively.

From microwave loss calculations, it is clear that loading the CPS line with PN junctions in the middle will increase the microwave loss by adding extra capacitance. The main advantage of the SPP configuration over the dual drive configuration is the reduced PN junction capacitance. This reduced capacitance will significantly reduce the microwave loss hence allowing SPP modulators to achieve higher bandwidth compared to dual drive modulators of the same length.

2.2.3 Velocity Matching

The last step in optimizing the traveling wave electrode is to minimize the mismatch between optical group velocity and microwave phase velocity. Due to the multilayered structure of the substrate, the presence of highly doped regions, and PN junctions, the substrate is subject to the “Maxwell–Wagner polarization effect” which in turn results in higher values of ε_{re} [29]. Therefore the microwave propagates along the electrode in a slow-wave mode. In this mode, because of the higher conductivity of the highly doped silicon regions, the electric field does not fully

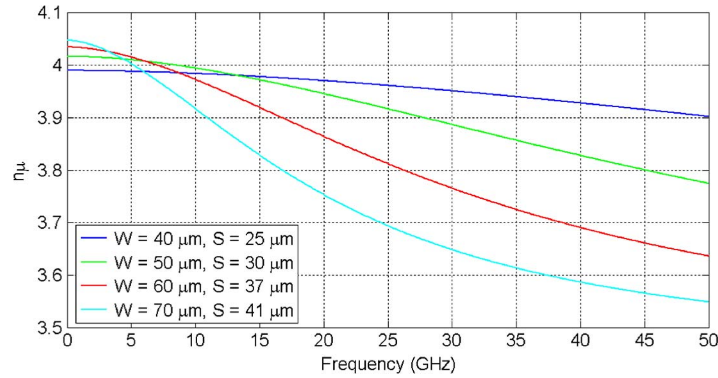

Fig. 5. Microwave effective refractive index versus frequency.

penetrate the silicon substrate and is predominantly confined in the oxide layer while the magnetic energy penetrates into the silicon substrate. This will result in the electric energy propagating along the interface of the oxide and silicon layers in significantly slower velocities [30].

The optical effective group index of the silicon waveguide is calculated using a mode solver software to be $n_{og} = 3.8$. The effective microwave index of CPS lines can be obtained from ε_{re}. It is clear from (2) and (3) that the microwave index is a function of frequency and CPS geometry. Fig. 5 illustrates the microwave effective refractive index $(n_\mu = \sqrt{\varepsilon_{re}})$ of the PN junction loaded CPS line as a function of frequency. It can be seen from Fig. 5 that for 60 μm wide electrodes with 37 μm spacing, the microwave refractive index value is within 5% of the optical group index for frequencies up to 50 GHz, indicating that good velocity matching can be achieved without the need for inductive or capacitive loaded electrode geometries.

The velocity mismatch limited, 3 dB bandwidth for a lossless impedance-matched modulator can be calculated as [26]

$$f_{3\text{ dB}} = \frac{1.4c}{\pi L |n_{og} - n_\mu|} \tag{9}$$

From (9) and Fig. 5, it is clear that velocity mismatch will not impact the bandwidth significantly as the difference between the optical group index and microwave phase index is less than 0.25 up to 50 GHz, corresponding to a 3 dB bandwidth of more than 100 GHz. Therefore, as shown in Section 2.2.2, the microwave loss is the main limiting factor of the frequency response of the modulator.

2.2.4 Final Design

The small signal electro-optic response of the modulator as a function of velocity mismatch and total microwave loss can be calculated by [26]

$$H(f) = e^{\frac{-\alpha L}{2}} \left[\frac{\sin^2\left(\frac{\alpha L}{2}\right) + \sin^2\left(\frac{\omega \Delta v L}{2}\right)}{\left(\frac{\alpha L}{2}\right)^2 + \left(\frac{\omega \Delta v L}{2}\right)^2} \right]^{\frac{1}{2}} \tag{10}$$

where Δv is the mismatch between the optical group velocity and microwave phase velocity, L is the length of the modulator, and α is the total microwave loss. Fig. 6 illustrates the simulated electro-optic S_{21} response of the modulator calculated using (10).

The CPS line designed is formed with a 2 μm thick aluminum layer using 60 μm wide traces separated with a 37 μm gap. This geometry provides a good tradeoff between microwave losses, velocity mismatch and impedance dispersion. The performance of narrower CPS geometries is limited by the conductor loss and wider traces are more prone to impedance dispersion and velocity mismatch.

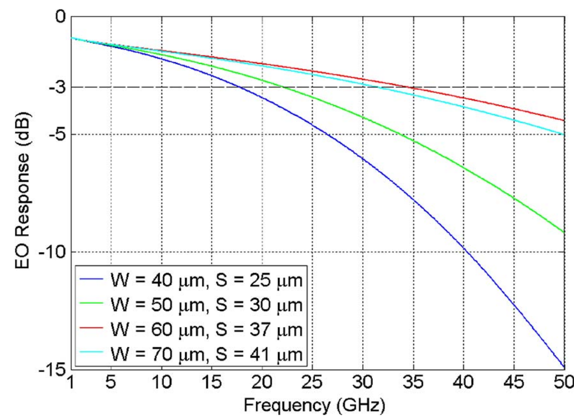

Fig. 6. Simulated small signal EO response of the modulator.

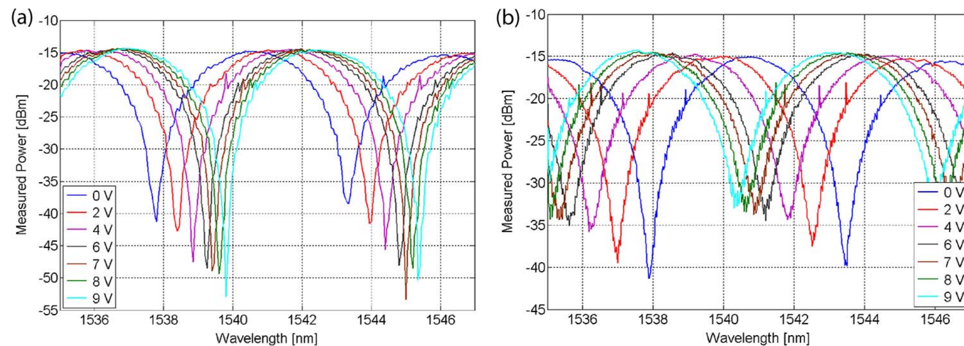

Fig. 7. Optical transmission spectrum for each arm of the modulator under various reverse bias voltages.

3. Device Characterization

The optical transmission spectrum for each arm of the MZM under different DC reverse bias voltages is shown in Fig. 7. The intentional imbalance in arms results in a transmission spectrum that is wavelength sensitive allowing the MZM to be characterized easily using a tunable laser and a photodetector. However, in commercial application balanced MZMs will be preferred due to their insensitivity to temperature and wavelength drifts. The V_π of each arm of the TW-MZM is observed to be 7.5 and 9.5 V, which corresponds to a $V_\pi L_\pi$ of 3.15 V-cm and 3.99 V-cm. The difference in $V_\pi L_\pi$ of each arm arises from the doping process variations and mask layer misalignments during fabrication. The observed 20 dB extinction ratio indicates a good balance of the optical power between the two arms of the TW-MZM. The on and off chip laser coupling was done through grating couplers. The fiber to fiber insertion loss to the SiP chip is measured to be 14.7 dB. After subtracting grating coupler losses and optical routing losses, the insertion loss of the MZM is found to be 4.5 dB.

A high frequency RF probe with a GSSG configuration is used to drive the transmission line and apply a 3 V DC bias and a SG probe is used to terminate the line with 50 Ω at the opposite end. The small signal properties of the TW-MZM are characterized using a 50 GHz lightwave component analyzer (LCA) at various DC bias voltages and are presented in Fig. 8(a)–(c). The curves are normalized to the response at a reference frequency of 1.5 GHz. A 35 GHz bandwidth is achieved under a 3 V bias voltage, surpassing any previously reported E-O bandwidth in a silicon modulator of comparable length by 5 GHz [12].

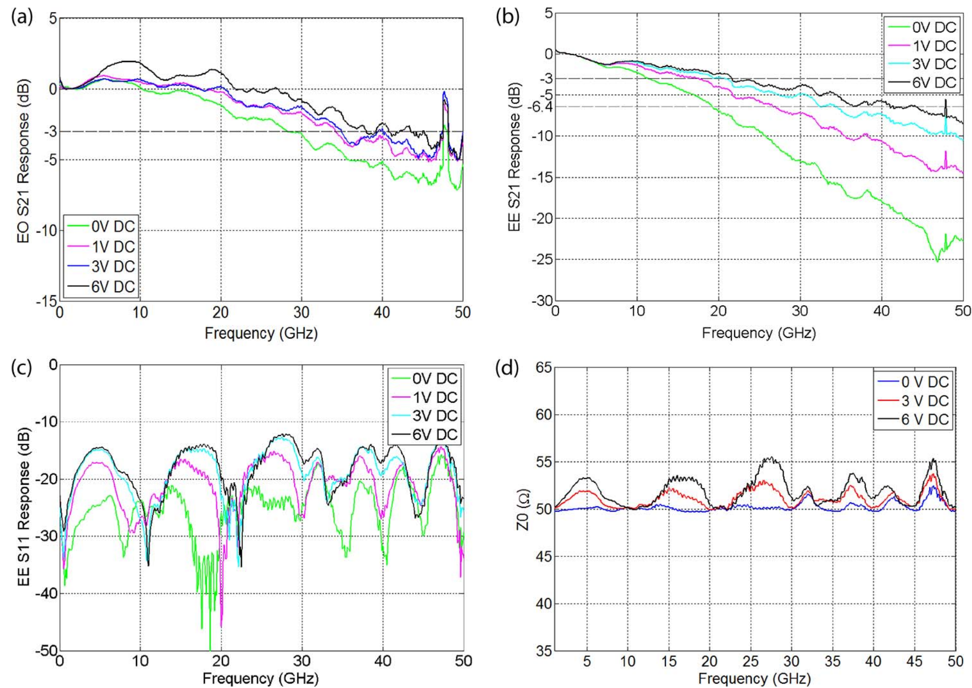

Fig. 8. (a) EO S_{21}, (b) EE S_{21}, (c) EE S_{11}, and (d) characteristic impedance of TW-MZM under various bias voltages versus frequency.

Fig. 8(d) demonstrates the extracted characteristic impedance of the TW-MZM from S-parameters under different bias voltages. The measured characteristic impedance has excellent agreement with the calculated results presented in Fig. 3(b), with less than 4% variations from the calculated values. The predicted impedance dispersion at higher frequencies is clearly observed in the measured results; however, over the 50 GHz frequency range, the impedance only varies by 2 Ω. Moreover the EE 6.4 dB and the EO 3 dB bandwidths shown are very close, indicating that the performance of the modulator is not limited by velocity mismatch [12]; this validates the design methodology outlined in Section 2. The observed EE S_{21} value of 21 GHz is lower than the calculated value of 25 GHz. This can be due to the neglected radiation losses and higher actual surface resistances.

Next, we examine the large signal performance of the modulator using an Agilent wide band oscilloscope. At the input of the modulator a tunable laser with maximum output power of 14 dBm is used. The modulator is operated at the quadrature point using the tunable laser. At this wavelength, the modulated signal power is -3.8 dBm and a 3 V DC bias voltage is applied using a RF probe to reverse bias the PN junctions. A $10^{31} - 1$ pseudorandom bit sequence (PRBS) signal generated by a SHF pulse pattern generator is amplified using a wide band microwave amplifier and attenuated by passive RF attenuators to obtain a 4.6 V_{pp} driving signal This signal is then applied to the modulator using a high-frequency RF probe. Fig. 9 shows eye diagrams for 30, 40, 50, and 55 Gb/s with extinction ratios of 11.58, 7.59, 5.35, and 4.30 and SNR of 10.31, 6.55, 4.32, and 3.18, respectively.

Eye diagrams, shown in Fig. 9, provide a visual qualitative presentation of the performance of the device. In order to quantitatively evaluate the performance of the modulator, bit error rate (BER) test of the system is performed. To do this, the input laser power to the modulator is set to 14.5 dBm. The output of the modulator is fed to an AC coupled Picometrix PD+TIA receiver which is then connected to a SHF bit error tester. An error-free ($\text{BER} < 10^{-12}$) operation up to 45 Gb/s is obtained with received power of -3.5 dBm, limited by the bandwidth of the PD+TIA receiver.

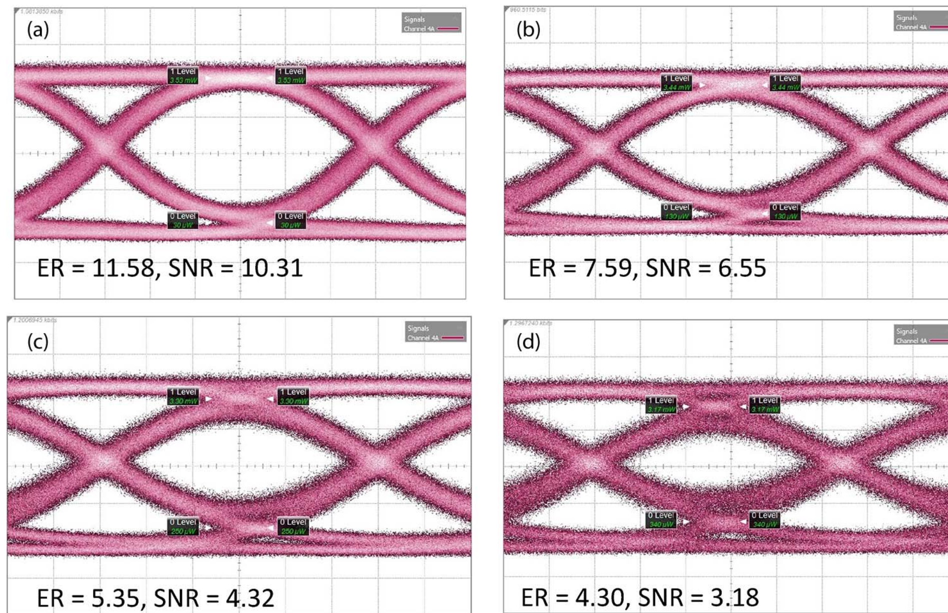

Fig. 9. Eye diagrams for (a) 30 Gb/s, (b) 40 Gb/s, (c) 50 Gb/s, and (d) 55 Gb/s on-off keying with extinction ratios of 11.58, 7.59, 5.35, and 4.30 and SNR of 10.31, 6.55, 4.32, and 3.18, respectively.

4. Transmission Experiments

The small optical insertion loss, together with the high optical extinction ratio of the transmission spectra and the high E-O bandwidth make this modulator an ideal transmitter for multilevel modulation formats. In this section we compare the performance of the modulator with PAM-2 and PAM-4 modulation formats over different lengths of fiber to reach a 100G Ethernet transport rate. At the input of the modulator, the same tunable laser with 14 dBm output power is used. The RF driving signal is generated using an AC coupled 8-bit Digital to Analog Converter (DAC) operating at 70 GSa/s. Use of a DAC allows us to apply digital signal processing (DSP) at the transmitter side. Four processes are applied to the waveform. First the symbol stream is up-sampled from one sample per symbol to $70/\mathrm{R_B}$, where $(\mathrm{R_B})$ is the desired symbol rate. Next a root raised cosine pulse shaping filter is applied. Thirdly, to equalize the spacing between modulated optical power levels, the nonlinearity of the power transfer function of the TW-MZM is compensated by applying an arcsin function to the waveform. Finally the frequency response of DAC, RF amplifier and TW-MZM cascade is pre-compensated by applying an inverse response function. An amplifier is used to amplify the DAC output to 2.2 V_{pp} which is then applied to the modulator using RF probes. The modulated signal is propagated through 1, 2, and 5 km of Corning SMF 28e+ fiber. The PD+TIA is used for opto-electrical (O-E) conversion before an Agilent real time oscilloscope serving as an 8-bit Analog to Digital converter (ADC) sampling at 80 GSa/s. At the receiver side, the digital signal processing is performed offline. First the signal is resampled from ADC rate of 80 GSa/s to twice the symbol rate $\mathrm{R_B}$. Next a matched filter defined at 2 samples per symbol is applied to the signal. The stream of samples is then filtered by a linear FIR filter. To recover the transmitter's clock and to apply symbol decision at the correct sampling instant, a digital clock recovery algorithm is implemented [7]. The output symbols are then used for error counting and to calculate the signal to noise ratio (SNR) and quality factor of the system. The DSP applied at the transmitter and receiver sides is discussed in detail in [7]. Fig. 10 illustrates the block diagram of the transmission system explained above.

We present the system performance qualitatively using eye diagrams and quantitatively by measuring BER and SNR. BER measurement is done by error counting. For PAM-N formats, SNR is defined as the ratio of the average signal power over average noise power. Fig. 11

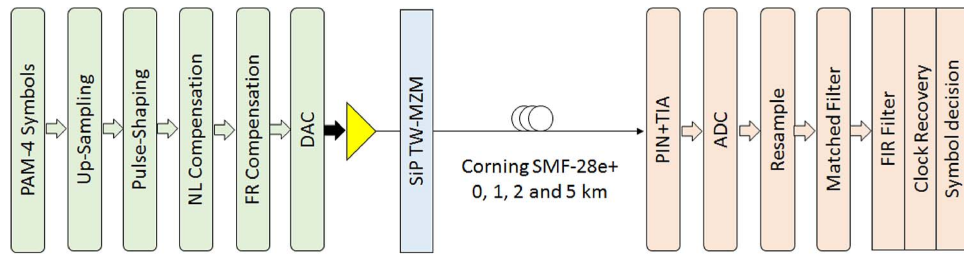

Fig. 10. Experimental setup.

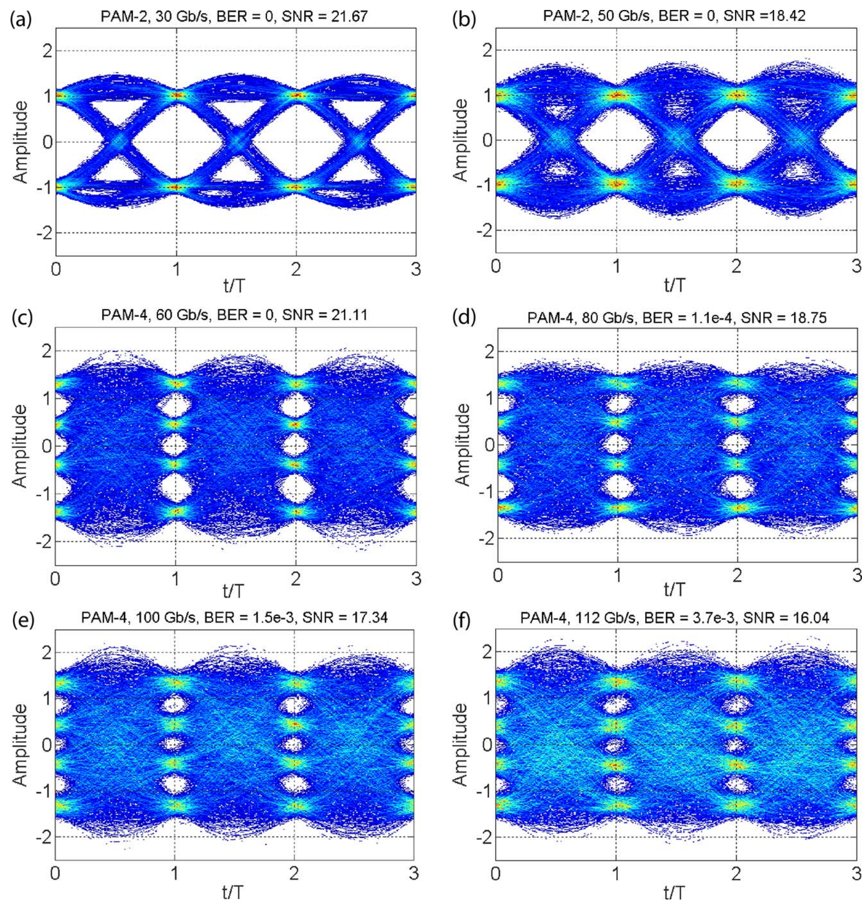

Fig. 11. Eye diagram after 2 km. (a) PAM-2 at 30 Gb/s, (b) PAM-2 at 50 Gb/s, (c) PAM-4 at 60 Gb/s, (d) PAM-4 at 80 Gb/s, (e) PAM-4 at 100 Gb/s, and (f) PAM-4 at 112 Gb/s.

shows eye diagrams for PAM-2 and PAM-4 formats at different baud rate after propagating through 2 km of fiber.

In currently deployed metro and long haul fiber optic transmission systems, Forward Error Correction (FEC) is used to significantly lower the BER. Based on OT4U standard [2], a client payload of 100 Gb/s is transmitted at line rate of 112 Gb/s, which includes 6.7% (FEC) over head. A BER measurement below the pre-BER threshold of 4.4×10^{-3} results in an output BER $< 10^{-15}$, viewed as error free transmission in the context of optical transmission. In this paper we assume FEC encoding and decoding at the transmitter and receiver side.

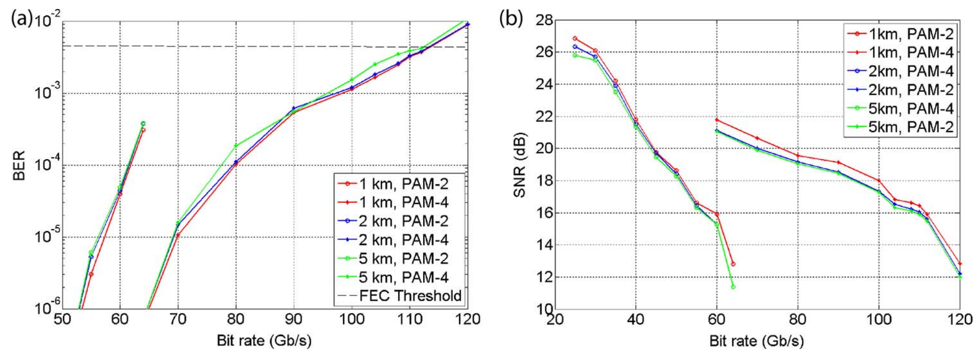

Fig. 12. (a) BER and (b) SNR of the system for PAM-2 and PAM-4 orders after propagating through 1, 2, and 5 km of SMF.

All eye diagrams are obtained after receiver DSP. A successful 100 Gb/s PAM-4 post-FEC error-free transmission through 2 km of fiber is achieved in all cases. After 5 km, for the same bit rate of fiber the pre-FEC BER is measured at 4×10^{-3} which is slightly lower than FEC threshold of 4.4×10^{-3}. For PAM-2, a maximum of 64 Gb/s transmission was achieved at pre-FEC BER of 1.31×10^{-4} which was limited by DAC's bandwidth.

Fig. 12 illustrates SNR and BER at various bit rates. We observe that, as the bit rate increases, the SNR and BER performance of the system degrades. The DAC has a 3 dB bandwidth of 15 GHz; however, using Nyquist sampling theory, the DAC can generate frequencies up to 35 GHz when sampling at 70 GSa/s. At higher bit rates the signal has higher frequency content. After digital compensation of the frequency response of the DAC, a signal of larger spectral content will have reduced V_{pp} swing out of the DAC, worsening the RF signal quality. At the receiver side, the same large bandwidth signal will integrate more inband noise power, further deteriorating the SNR. The cumulative effect of transmitter and receiver signal worsening as the symbol rate increases is observed in Fig. 12.

The low insertion loss of the device allowed the full operation of the modulator without the need for optical amplifiers, which further differentiates this work from other modulators presented in the literature [5], [7], [12].

5. Conclusion

In this paper, we present the design and characterization of a low voltage silicon photonic traveling wave modulator. A thorough analysis of the implemented traveling wave electrode is presented. It is shown that using a CPS geometry, it is possible to minimize the mismatch between the microwave phase velocity and optical group velocity by careful design. As a result, the main bandwidth limiting factor is determined to be the microwave loss. A 3 dB electro-optic bandwidth of 35 GHz under 3 V DC bias is demonstrated. We further investigate the performance of the device in a short reach transmission system. By applying digital signal processing on transmitter and the receiver side we obtain a successful 112 Gb/s transmission of 4 level pulse amplitude modulation over 5 km of SMF below pre-FEC hard decision threshold of 4.4×10^{-3}. We present an alternative solution to 4×25 Gb/s WDM transmission systems. We demonstrate that higher modulation formats such as PAM-4, together with digital signal processing can be used to achieve 100 Gb/s transmission on a single wavelength.

Acknowledgement

The authors gratefully acknowledge CMC Microsystems for enabling fabrication and providing access to simulation and CAD tools.

References

[1] G. Ghione, *Semiconductor Devices for High-Speed Optoelectronics*. Cambridge, U.K.: Cambridge Univ. Press, 2009.
[2] *Media Access Control Parameters, Physical Layers, and Management Parameters for 40 Gb/s and 100 Gb/s Operation*, IEEE Std. 802.3ba, Approved by IEEE and ANSI on Jun. 17, 2010. [Online]. Available: http://standards.ieee.org/findstds/standard/802.3ba-2010.html
[3] *400 GbE Task Force*, IEEE P802.3bs. [Online]. Available: http://www.ieee802.org/3/bs/public/14_05/index.shtml
[4] M. Morsy-Osman *et al.,* "Analytical and experimental performance evaluation of an integrated Si-photonic balanced coherent receiver in a colorless scenario," *Opt. Exp.*, vol. 22, no. 5, pp. 5693–5730, Mar. 2014.
[5] P. Dong, C. Xie, L. Chen, L. Buhl, and Y. Chen, "112-Gb/s monolithic PDM-QPSK modulator in silicon," *Opt. Exp.*, vol. 20, no. 26, pp. B624–B629, Dec. 2012.
[6] J. Klamkin *et al.,* "A 100-Gb/s noncoherent silicon receiver for PDM-DBPSK/DQPSK signals," *Opt. Exp.*, vol. 22, no. 2, pp. 2150–2158, Jan. 2014.
[7] M. Chagnon *et al.,* "Experimental study of 112 Gb/s short reach transmission employing PAM formats and SiP intensity modulator at 1.3 μm," *Opt. Exp.*, vol. 22, no. 17, pp. 21018–21036, Aug. 2014.
[8] M. Streshinsky *et al.,* "Low power 50 Gb/s silicon traveling wave Mach–Zehnder modulator near 1300 nm," *Opt. Exp.*, vol. 21, no. 25, pp. 30350–30357, Dec. 2013.
[9] P. Dong, C. Xie, L. Chen, N. Fontaine, and Y. Chen, "Experimental demonstration of microring quadrature phase-shift keying modulators," *Opt. Lett.*, vol. 37, no. 7, pp. 1178–1180, Apr. 2012.
[10] A. Samani *et al.,* "OOK and PAM optical modulation using a single drive push pull silicon Mach–Zehnder modulator," in *Proc. IEEE 11th Int. Conf. GFP*, Aug. 27–29, 2014, pp. 45–46.
[11] X. Wu *et al.,* "A 20 Gb/s NRZ/PAM-4 1 V transmitter in 40 nm CMOS driving a Si-photonic modulator in 0.13 μm CMOS," in *Proc. IEEE ISSCC*, pp. 128–129, Feb. 17–21, 2013.
[12] R. Ding *et al.,* "Design and characterization of a 30-GHz bandwidth low-power silicon traveling-wave modulator," *Opt. Commun.*, vol. 321, pp. 124–133, 2014.
[13] M. Scholten, T. Coe, and J. Dillard, "Continuously-interleaved BCH (CI-BCH) FEC delivers best in class NECG for 40G and 100G metro applications," in *Proc. OFC*, San Diego, CA, USA, 2010, pp. 1–3.
[14] P. Dong, L. Chen, and Y. Chen, "High-speed low-voltage single-drive push–pull silicon Mach–Zehnder modulators," *Opt. Exp.*, vol. 20, no. 6, pp. 6163–6169, Mar. 2012.
[15] T. Baehr-Jones *et al.,* "Ultralow drive voltage silicon traveling-wave modulator," *Opt. Exp.*, vol. 20, no. 11, pp. 12014–12020, May 2012.
[16] H. Yu and W. Bogaerts, "An equivalent circuit model of the traveling wave electrode for carrier-depletion-based silicon optical modulators," *J. Lightw. Technol.*, vol. 30, no. 11, pp. 1602–1609, Jun. 2012.
[17] B. Yang, X. Shao, N. Goldsman, and O. Ramahi, "Modeling RF signal propagation along on-chip interconnects and the effect of substrate doping with the alternating-direction-implicit finite-difference time-domain (ADI-FDTD) method," in *Proc. Power Modulator Symp.*, Arlington, VA, USA, 2006, pp. 170–173.
[18] R. Walker, "High-speed III–V semiconductor intensity modulators," *IEEE J. Quantum Electron.*, vol. 27, no. 3, pp. 654–667, Mar. 1991.
[19] L. Zhu, "Guided-wave characteristics of periodic coplanar waveguides with inductive loading-unit-length transmission parameters," *IEEE Trans. Microw. Theory Techn.*, vol. 51, no. 10, pp. 2133–2138, Oct. 2003.
[20] R. Ding *et al.,* "High-speed silicon modulator with slow-wave electrodes and fully independent differential drive," *IEEE J. Lightw. Technol.*, vol. 32, no. 12, pp. 2240–2247, Jun. 2014.
[21] J. Shin, S. Sakamoto, and N. Dagli, "Conductor loss of capacitively loaded slow wave electrodes for high-speed photonic devices," *J. Lightw. Technol.*, vol. 29, no. 1, pp. 48–52, Jan. 2011.
[22] J. Liou and K. Lau, "Analysis of slow-wave transmission lines on multi-layered semiconductor structures including conductor loss," *IEEE Trans. Microw. Theory Techn.*, vol. 41, no. 5, pp. 824–829, May 1993.
[23] R. Garg, I. Bahl, and M. Bozzi, *Microstrip Lines and Slotlines*, 3rd ed. Norwood, MA, USA: Artech House, 2013.
[24] E. Chen and S. Chou, "Characteristics of coplanar transmission lines on multilayer substrates: Modeling and experiments," *IEEE Trans. Microw. Theory Techn.*, vol. 45, no. 6, pp. 939–945, Jun. 1997.
[25] J. Zheng, Y.-C. Hahm, V. Tripathi, and A. Weisshaar, "CAD-oriented equivalent-circuit modeling of on-chip interconnects on lossy silicon substrate," *IEEE Trans. Microw. Theory Techn.*, vol. 48, no. 9, pp. 1443–1451, Sep. 2000.
[26] H. Chung, W. Chang, and E. Adler, "Modeling and optimization of traveling-wave $LiNbO_3$ interferometric modulators," *IEEE J. Quantum Electron.*, vol. 27, no. 3, pp. 608–617, Mar. 1991.
[27] P. Majumdar and A. Verma, "CAD models of losses for symmetric elliptical and circular cylindrical coplanar strip lines," *Int. J. Electron.*, vol. 98, no. 7, pp. 863–882, 2011.
[28] C. Schollhorn, W. Zhao, M. Morschbach, and E. Kasper, "Attenuation mechanisms of aluminum millimeter-wave coplanar waveguides on silicon," *IEEE Trans. Electron Devices*, vol. 50, no. 3, pp. 740–746, Mar. 2003.
[29] D. Lederer and J. Raskin, "Substrate loss mechanisms for microstrip and CPW transmission lines on lossy silicon wafers," *Solid-State Electron.*, vol. 47, no. 11, pp. 1927–1936, 2003.
[30] B. Yang, S. Xi, N. Goldman, and O. Ramahi, "Full wave modeling of substrate doping effects and nonideal conductors in integrated circuit interconnects," in *Proc. Int. Semicond. Device Res. Symp.*, Bethesda, MD, USA, 2005, pp. 368–369.